Relativistic calculation of Lβ_2 satellite spectra of W and Au

J.P. Marques[1,a], F. Parente[1,b], M.C. Martins[1], and P. Indelicato[2]

[1] Centro de Física Atómica e Departamento Física, Faculdade de Ciências, Universidade de Lisboa, Campo Grande,
Ed. C8, 1749-016 Lisboa, Portugal

[2] Laboratoire Kastler Brossel, École Normale Supérieure, CNRS, Université P. et M. Curie, Paris VI, Case 74,
4 place Jussieu, 75252 Paris Cedex 05, France

Abstract. Lβ_2 X-ray satellite spectra of tungsten and gold are calculated using the Multi-Configuration Dirac-Fock energies and compared with recent experimental data. New calculations of L_1-L_3M_5 Coster-Kronig transition energies for tungsten are presented, confirming the origin of the Lβ_2 visible satellites reported by two experimental groups. We found the value 5.09 eV for the average energy of the L_1-L_3M_5 Coster-Kronig transition in tungsten. The Lβ_2 satellite spectrum of tungsten was calculated in the framework of a statistical model, which makes use of Racah's algebra. A detailed calculation of the Lβ_2 and Lβ_{15} satellite spectra was performed for gold.

PACS. 32.30.Rj X-ray spectra – 32.70.Fw Absolute and relative intensities – 32.80.Hd Auger effect and inner-shell excitation or ionization

1 Introduction

X-ray lines from almost neutral atoms are seldom pure, being in most cases contaminated by the so-called satellite lines, that is, X-ray lines that result from transitions in multi-inner hole atomic configurations. In heavy atoms, X-ray lines resulting from L → M, N hole transitions with a M spectator hole lead, in general, to satellites that can be resolved from the diagram line (visible satellites), whereas the ones with N-, O- or P-shell spectator holes usually appear embedded within the natural width of the parent line (hidden satellites).

The study of X-ray satellite lines in systems where only one spectator inner hole exists is more than seventy years old, yet not very many works on this subject have been published. Ritchmeyer and Ramberg [1] compared their computed satellite structure of L$\alpha_{1,2}$ (L$_3$ → M$_{4,5}$ hole transitions), Lβ_2 (L$_3$ → N$_5$) and Lβ_{15} (L$_3$ → N$_4$) spectra for gold with experimental data. Lα X-ray satellite spectra of elements between Zr and Cd were studied by Juslén et al. [2]. Doyle and Shafroth [3] measured the intensities of Lα and Lβ_1 (L$_2$ → M$_4$) satellites of elements in the $37 \le Z \le 56$ region. Hague et al. [4] reported on

[a] e-mail: jmmarques@fc.ul.pt

[b] *Present address*: Departamento de Física, Faculdade de Ciências e Tecnologia, Universidade Nova de Lisboa, Monte de Caparica, 2829-516 Caparica, Portugal.

silver Lα satellites. Extensive tables of relativistic energies of L X-ray satellite lines, using the Dirac-Fock-Slater (DFS) approach including quantum electrodynamic corrections, were published by Parente et al. [5]. The Lα_1 satellite structures of iridium, gold and uranium were studied theoretically by Parente et al. [6] and experimentally by Carvalho et al. [7]. The possibility that L X-ray satellite lines, not predicted by theory, could be present in tungsten was raised by Salgueiro et al. [8], to explain their experimental data. A simple model to study the relative intensities of satellite and diagram X-ray lines following L-shell ionization in the region around $Z = 50$ was proposed by Xu and Rosato [9]. Most recently, Vlaicu et al. [10] studied the L emission spectrum of tungsten, confirming the existence of the satellite lines found by Salgueiro et al. [8], and later Oohashi et al. [11] focused on the origin of the Lβ_2 visible satellite lines in gold.

The existence of satellite lines in X-ray spectra has been explained long ago by the creation of multiple vacancies in inner-shells, resulting from the ionization process. Two mechanisms have been proposed for the creation of double vacancies after a primary ionization in the L_1 or L_2 subshells, namely shake-off and L_i-L_jX_k Coster-Kronig transitions. Here $i = 1, 2$, $j = 2, 3$ (with $i \ne j$), and X_k may be any outer subshell. The shake process, for energies not far above the threshold, depends on the excitation energy [12], whereas Coster-Kronig transitions are independent on the excitation energy. Furthermore,

Coster-Kronig transitions are highly probable when energetically allowed so that, in this case, the atom, after the primary ionization, will unavoidably end up with two inner-shell vacancies.

Atomic K- and L-shells relativistic radiationless transition probabilities for 22 elements with atomic numbers $18 \leq Z \leq 96$ were published in 1979 by Chen et al. [13]. Earlier, in 1977, the same authors had found L_1-$L_3M_{4,5}$ Coster-Kronig transitions to be energetically forbidden in the region $50 \leq Z \leq 79$ [14]. However, in 1987, Salgueiro et al. [8] obtained tungsten $L\alpha$ X-ray spectra where satellite lines were present, which could not be explained by the shake mechanism. Therefore they suggested that, most probably, Coster-Kronig L_1-L_3M_5 transitions could take place in tungsten, contrary to Chen et al. predictions. The existence of these satellite lines was confirmed in 1998 by Vlaicu and co-workers [10]. We note, however, that Agarwal [15] already referred the existence of L_1-L_3M_5 Coster-Kronig transitions for $Z > 73$ in 1979.

In this work we used the multi-configuration Dirac-Fock code of Desclaux and Indelicato [16–18] to calculate the energies of L_1- and $L_3M_{4,5}$-hole levels of tungsten, looking for the possibility of existence of L_1-$L_3M_{4,5}$ Coster-Kronig transitions. Our results led to the conclusion that L_1-L_3M_5 transitions are indeed energetically allowed in tungsten, contrary to Chen et al. [14] prediction. Furthermore, we used the same code to compute transition energies of the X-ray lines in the $L\beta_2$ satellite band of tungsten. As the number of lines involved is too big to handle, we used the method suggested by Parente et al. [5], using Racah's algebra, to predict the shape of this satellite band.

The $L\beta_2$ and $L\beta_{15}$ satellite bands of gold, where the number of transitions allows for a full calculation, were also studied in this work and compared with recent experimental results [11]. Spectator holes in all possible subshells were considered in the study, including the ones that give origin to hidden satellites. To assess the accuracy of the method that makes use of Racah's algebra, we also used this method for gold, to allow for a comparison with the results of the full calculation.

2 Calculation of atomic wave functions and transition probabilities

Bound states wave functions are calculated using the Dirac-Fock program of Desclaux and Indelicato. Details on the Hamiltonian and the processes used to build the wave-functions can be found elsewhere [16,17,19].

The total wave function is calculated with the help of the variational principle. The total energy of the atomic system is the eigenvalue of the equation

$$\mathcal{H}^{\text{no pair}}\Psi_{\Pi,J,M}(\ldots,\boldsymbol{r}_i,\ldots) = E_{\Pi,J,M}\Psi_{\Pi,J,M}(\ldots,\boldsymbol{r}_i,\ldots),$$
(1)

where Π is the parity, J is the total angular momentum eigenvalue, and M is the eigenvalue of its projection on

the z-axis J_z. Here,

$$\mathcal{H}^{\text{no pair}} = \sum_{i=1}^{N} \mathcal{H}_D(r_i) + \sum_{i<j} V_{ij},$$
(2)

where $\mathcal{H}_D$ is the one electron Dirac operator and V_{ij} is an operator representing the electron-electron interaction of order one in α. The expression of V_{ij} in the Coulomb gauge and in atomic units is

$$V_{ij} = \frac{1}{r_{ij}}$$
(3a)

$$-\frac{\boldsymbol{\alpha}_i \cdot \boldsymbol{\alpha}_j}{r_{ij}}$$
(3b)

$$-\frac{\boldsymbol{\alpha}_i \cdot \boldsymbol{\alpha}_j}{r_{ij}} \left[\cos\left(\frac{\omega_{ij}r_{ij}}{c}\right) - 1\right]$$

$$+ c^2(\boldsymbol{\alpha}_i \cdot \boldsymbol{\nabla}_i)(\boldsymbol{\alpha}_j \cdot \boldsymbol{\nabla}_j)\frac{\cos\left(\frac{\omega_{ij}r_{ij}}{c}\right) - 1}{\omega_{ij}^2 r_{ij}},$$
(3c)

where $r_{ij} = |\boldsymbol{r}_i - \boldsymbol{r}_j|$ is the inter-electronic distance, ω_{ij} is the energy of the exchanged photon between the two electrons, $\boldsymbol{\alpha}_i$ are the Dirac matrices and c is the speed of light. We use the Coulomb gauge as it has been demonstrated that it provides energies free from spurious contributions at the ladder approximation level and must be used in many-body atomic structure calculations [20,21].

The term (3a) represents the Coulomb interaction, the term (3b) is the Gaunt (magnetic) interaction, and the last two terms (3c) stand for the retardation operator. In this expression the $\boldsymbol{\nabla}$ operators act only on r_{ij} and not on the following wave functions.

By a series expansion of the operators in expressions (3b) and (3c) in powers of $\omega_{ij}r_{ij}/c \ll 1$ one obtains the Breit interaction, which includes the leading retardation contribution of order $1/c^2$. The Breit interaction is, then, the sum of the Gaunt interaction (3b) and the Breit retardation

$$B_{ij}^{\text{R}} = \frac{\boldsymbol{\alpha}_i \cdot \boldsymbol{\alpha}_j}{2r_{ij}} - \frac{(\boldsymbol{\alpha}_i \cdot \boldsymbol{r}_{ij})(\boldsymbol{\alpha}_j \cdot \boldsymbol{r}_{ij})}{2r_{ij}^3}.$$
(4)

In the many-body part of the calculation the electron-electron interaction is described by the sum of the Coulomb and the Breit interactions. Higher orders in $1/c$, deriving from the difference between equations (3c) and (4) are treated here only as a first order perturbation. All calculations are done for finite nuclei using a Fermi distribution with a thickness parameter of 2.3 fm. The nuclear radii are taken from reference [22].

The MCDF method is defined by the particular choice of a trial function to solve equation (1) as a linear combination of configuration state functions (CSF):

$$|\Psi_{\Pi,J,M}\rangle = \sum_{\nu=1}^{n} c_\nu |\nu, \Pi, J, M\rangle.$$
(5)

The CSF are also eigenfunctions of the parity Π, the total angular momentum J^2 and its projection J_z. The label ν

stands for all other numbers (principal quantum number, ...) necessary to define unambiguously the CSF. The c_ν are called the mixing coefficients and are obtained by diagonalization of the Hamiltonian matrix coming from the minimization of the energy in equation (5) with respect to the c_ν. The CSF are antisymmetric products of one-electron wave functions expressed as linear combination of Slater determinants of Dirac 4-spinors

$$|\nu, \Pi, J, M\rangle = \sum_{i=1}^{N_\nu} d_i \begin{vmatrix} \psi_1^i(r_1) & \cdots & \psi_m^i(r_1) \\ \vdots & \ddots & \vdots \\ \psi_1^i(r_m) & \cdots & \psi_m^i(r_m) \end{vmatrix}. \quad (6)$$

where the ψ-s are the one-electron wave functions and the coefficients d_i are determined by requiring that the CSF is an eigenstate of J^2 and J_z. A variational principle provides the integro-differential equations to determine the radial wave functions and a Hamiltonian matrix that provides the mixing coefficients c_ν by diagonalization. One-electron radiative corrections (self-energy and vacuum polarization) are added afterwards. All the energies are calculated using the experimental nuclear charge distribution for the nucleus.

The so-called Optimized Levels (OL) method was used to determine the wave function and energy for each state involved. Thus, spin-orbitals in the initial and final states are not orthogonal, since they have been optimized separately. The formalism to take in account the wave functions non-orthogonality in the transition probabilities calculation has been described by Löwdin [23]. The matrix element of a one-electron operator O between two determinants belonging to the initial and final states can be written

$$\langle \nu \Pi J M| \sum_{i=1}^{N} O(r_i) |\nu'\Pi'J'M'\rangle =$$
$$\frac{1}{N!} \begin{vmatrix} \psi_1(r_1) & \cdots & \psi_m(r_1) \\ \vdots & \ddots & \vdots \\ \psi_1(r_m) & \cdots & \psi_m(r_m) \end{vmatrix}$$
$$\times \sum_{i=1}^{m} O(r_i) \begin{vmatrix} \phi_1(r_1) & \cdots & \phi_m(r_1) \\ \vdots & \ddots & \vdots \\ \phi_1(r_m) & \cdots & \phi_m(r_m) \end{vmatrix}, \quad (7)$$

where the ψ_i belong to the initial state and the ϕ_i and primes belong to the final state. If $\psi = |n\kappa\mu\rangle$ and $\phi = |n'\kappa'\mu'\rangle$ are orthogonal, i.e., $\langle n\kappa\mu|n'\kappa'\mu'\rangle = \delta_{n,n'}\delta_{\kappa,\kappa'}\delta_{\mu,\mu'}$, the matrix element (7) reduces to one term $\langle \psi_i| O |\phi_i\rangle$ where i represents the only electron that does not have the same spin-orbital in the initial and final determinants. Since O is a one-electron operator, only one spin-orbital can change, otherwise the matrix element is zero. In contrast, when the orthogonality between initial and final

states is not enforced, one gets [23]

$$\langle \nu \Pi J M| \sum_{i=1}^{N} O(r_i) |\nu'\Pi'J'M'\rangle = \sum_{i,j'} \langle \psi_i| O |\phi_{j'}\rangle D_{ij'}, \quad (8)$$

where $D_{ij'}$ is the minor determinant obtained by crossing out the ith row and j'th column from the determinant of dimension $N \times N$, made of all possible overlaps $\langle \psi_k|\phi_{l'}\rangle$.

Radiative corrections are also introduced, from a full QED treatment. The one-electron self-energy is evaluated using the one-electron values of Mohr and coworkers [24–26] and corrected for finite nuclear size [27]. The self-energy screening and vacuum polarization are treated with an approximate method developed by Indelicato and coworkers [28–31].

3 Results

3.1 Tungsten

Using the MCDF code of Desclaux and Indelicato [16,17], we calculated the energies of all levels in the L_1- and L_3M_5-hole configurations of tungsten, to check for the possibility of Coster-Kronig transitions between these two configurations. Interaction of the inner holes with electrons in outer unfilled shells was taken in account and full relaxation was included but no electronic correlation.

There are 63 energy levels in the L_1 configuration. We found 359 energy levels in the L_3M_5 configuration with energies below the lowest energy level of the L_1 configuration. Thus, we arrive to the conclusion that L_1-L_3M_5 Coster-Kronig transitions are indeed possible in tungsten, originating the double L_3M_5 vacancy state which afterwards yield the satellite lines first detected by Salgueiro et al. [8] and confirmed by Vlaicu et al. [10]. Averaging over initial and final state energies, we found for the radiationless transition the energy of 5.09 eV.

This value is to be compared to -2.70 eV found by Chen et al. [14], using a relativistic DFS approach. In the latter work coupling with unfilled outer shells was neglected. These authors present the Coster-Kronig transition energies as differences of initial and final average total system energies, which does not allow for a detailed comparison between individual level energies.

Using the MCDF computer code, we calculated the energies of all possible $L_3 \rightarrow N_5$ radiative transitions in the presence of a M_5 spectator hole and four $5d$ electrons in the outer unfilled shell, L_3M_5-M_5N_5 transitions, that yield the $L\beta_2$ satellite band. In general, to each pair of initial and final angular momenta correspond several X-ray transitions. A full calculation of transition probabilities would be, in this case, a formidable task, due to the enormous number, more than one hundred thousand, of authorized transitions. Instead, we used Racah's algebra to compute the relative line intensities, using the method of Parente

et al. [5]. This method assumes:

1. the initial multiplet states are populated statistically;
2. the effect of the multiplet energy differences on the X-ray matrix elements can be neglected;
3. the Auger decay rates of the various multiplet states of a configuration can be taken to be identical. In fact, for heavy atoms there are so many open Auger channels that the multiplet effect on Auger emission rates for double-hole states becomes minimal.

The angular momenta resulting from the unfilled shells are j_1, j_2, j_3 and j_1', j_2', j_3' for the initial and final configurations, respectively, where j_3 and j_3' refer to the outer unfilled shell electrons.

Under the above assumptions, the intensity for the line

$$|j_1 j_2(J_{12}), j_3; J\rangle \rightarrow |j_1' j_2'(J_{12}'),\ j_3'; J'\rangle$$

is found to be proportional to

$$\left| \sum_{J_{13}'} (2J_{13}'+1) \sqrt{(2J_{12}'+1)(2J_{12}+1)(2J'+1)(2J+1)} \right.$$
$$\times \sqrt{(2j_1+1)(2j_2'+1)}$$
$$\times (-1)^{J_{12}'+j_3'+3J_{13}'+j_2'+3j_1+j_2+j_3+J'+1}$$
$$\left. \times \left\{ \begin{matrix} J_{12}' & j_3' & J' \\ J_{13}' & j_2' & j_1' \end{matrix} \right\} \left\{ \begin{matrix} j_1 & j_2 & J_{12} \\ j_3 & J & J_{13}' \end{matrix} \right\} \left\{ \begin{matrix} j_2' & J' & J_{13}' \\ J & j_1 & 1 \end{matrix} \right\} \right|^2, \quad (9)$$

where J_{ik} results from the coupling between angular momenta j_i and j_k. In what concerns the L_3M_5-M_5N_5 transitions, we have $j_1 = 3/2$; $j_2 = j_2' = 5/2$; $j_1' = 5/2$. For tungsten the coupling of the four $5d$ electron angular momenta yields $j_3 = 0, \ldots, 6$; $j_3' = 0, \ldots, 6$; $J = 0, \ldots, 10$; $J' = 0, \ldots, 11$. For each pair of J, J' values, the remaining angular momenta values can be found using standard angular momenta calculations.

Only one energy value for each total angular momentum J is considered. This method will then reproduce the sum of the contributions of the several components of the $J \rightarrow J'$ transition, within the approximations stated above. Thus, we assumed only one line for each pair of initial and final angular momenta values, assigning to this line the weighted energy and the sum of the line component intensities, in arbitrary units. As L_3M_5-M_5N_4 transition lines are much less intense that L_3M_5-M_5N_5 lines, we did not include them in the calculation for tungsten.

We assume that the natural width of the L_3M_5-M_5N_5 satellite line is given by [14]

$$\Gamma(L_3M_5\text{-}M_5N_5) = \Gamma_{L_3}^{tot} + 2\Gamma_{M_5}^{tot} + \Gamma_{N_5}^{tot}, \quad (10)$$

where Γ_X^{tot} is the natural width of X level. Using the values proposed by Campbell and Papp [32] we obtained 12.2 eV for the width of each of those satellite lines. In this way we arrived at the tungsten $L\beta_2$ satellite band presented in Figure 1, together with the corresponding spectrum generated using the DFS energy values of Parente et al. [5].
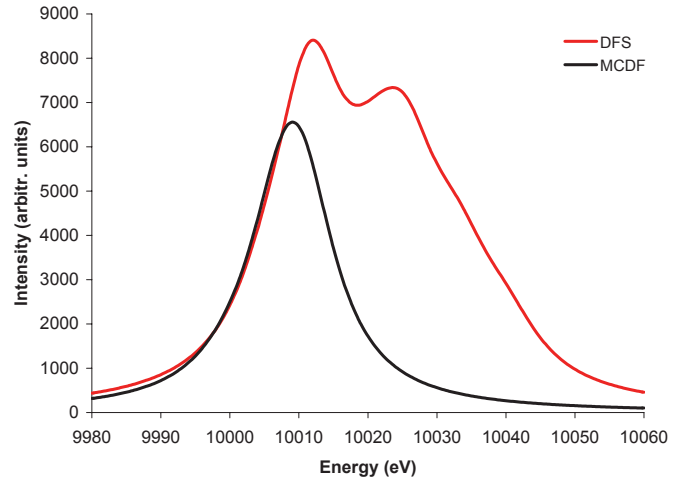

Fig. 1. Calculated $L\beta_2$ satellite band of tungsten, using Dirac-Fock-Slater - DFS [5], and Multi-Configuration Dirac-Fock - MCDF (this work) energy values, respectively. In both cases, relative intensities were calculated in the present work using Racah's algebra, as described in the text. The bands are normalized in intensity.

Due to the fact that only the lowest levels of the initial L_3M_5 hole configuration are fed by Coster-Kronig transitions from the L_1 hole initial configuration, the theoretical X-ray satellite band generated in this work is much narrower than if all initial levels were fed. This is clearly shown in Figure 1, as the satellite band computed using DFS energy values included all energy levels of the L_3M_5 configuration as initial levels.

This prediction can be compared with the experimental data of Vlaicu et al. (Fig. 2 of [10]). Although the data resolution is very poor, for obvious lack of statistics, the proeminent peak with energy around 10010 eV is well reproduced in the theoretical band (Fig. 1 - MCDF). It is obvious that experimental results with better statistics are needed.

Vlaicu et al. [10] estimated relative intensities of the L-satellite lines for tungsten, using the expressions proposed by Xu and Rosato [9], following the model of Krause et al. [33], with values obtained by other authors for the pertinent quantities. As they used Chen et al. [14] results for the Coster-Kronig transition probabilities, they assumed that the Coster-Kronig channel for creating M-shell spectator holes is closed, contrary to the findings of the present work.

3.2 Gold

3.2.1 Coster-Kronig transition energies

The $L\beta_2$ and $L\beta_{15}$ satellite bands of gold were studied in this work. In this case, the existence of both L_1-L_3M_4 and L_1-L_3M_5 Coster-Kronig transitions were predicted by Chen et al. [14] and confirmed by our own calculation.

Table 1. Energies in eV and transition probabilities (W) in s^{-1} for gold Lβ_2, Lβ_{15}, and Lβ_3 diagram lines.

L$_3$ - N$_5$ (Lβ_2)		L$_3$ - N$_4$ (Lβ_{15})		L$_1$ - M$_3$ (Lβ_3)	
Energy	W	Energy	W	Energy	W
11581.36	1.38×10^{14}	11563.24	1.28×10^{13}	11612.24	1.67×10^{14}
11581.33	1.54×10^{13}	11563.20	2.66×10^{12}	11611.82	8.31×10^{13}
11581.40	2.14×10^{14}	11563.21	2.55×10^{12}	11611.87	4.15×10^{14}
		11563.17	2.28×10^{13}		

We found for the L$_1$-L$_3$M$_4$ Coster-Kronig transition in gold the energy of 38.23 eV and for the L$_1$-L$_3$M$_5$ transition the energy of 132.15 eV. These values are close to the 37.65 eV and 130.39 eV values, respectively, obtained by Chen et al. [13].

The theoretical Lβ_2 satellite band of gold was obtained by calculating the transition probabilities for all possible dipolar electric transitions corresponding to the decay of the L$_3$M$_5$ and L$_3$M$_4$ double-hole configurations, in the energy window between 11600–11700 eV, and, in a separate way, using Racah's algebra method, as was done for tungsten.

3.2.2 Full MCDF calculation of satellite band

In gold, 8 and 7 energy levels correspond to the L$_3$M$_5$- and L$_3$M$_4$-hole configurations respectively. On the other hand, 11 and 8 levels correspond to the M$_5$N$_5$ and M$_4$N$_5$ configurations. This leads to 78 possible electric-dipole allowed lines between the levels of the L$_3$M$_{4,5}$ and M$_{4,5}$N$_5$ configurations that yield the Lβ_2 visible satellite band. The calculations of the energies and transition probabilities for these lines were performed using the MCDF code of Desclaux and Indelicato, in single-configuration mode, which includes all relativistic CSF originated from a single LS configuration.

The Lβ_{15} (L$_3$M$_{4,5}$-M$_{4,5}$N$_4$) visible satellite lines, although much less intense than the previous ones, also exist in the same energy window. So, we included these lines in our calculation.

Results for transition energies and probabilities of Lβ_2, Lβ_{15} and Lβ_3 (L$_1 \rightarrow$ M$_3$) diagram lines are presented in Table 1. Transition energies and probabilities for Lβ_2 and Lβ_{15} visible satellite lines are shown in Table 2.

Furthermore, satellite lines originating from double-holes, in L$_3$ and N, O, or P subshells, have energies that are embedded in the natural widths of the diagram lines. So, the corresponding transition energies and probabilities have also been calculated.

In order to compare MCDF calculations of transition energies and probabilities with experiment, we have to know the X-ray production cross-sections for lines arising from single- and double-hole states in gold. The pertinent expressions can be found in Xu and Rosato [9], using the model of Krause et al. [33].

We define the cross-section for creation of a single-hole configuration in the L$_i$ subshell as

$$\sigma'_{L_i} = \sigma_{L_i}(1 - Q_{L_i}), \tag{11}$$

whereas for the L$_3$X ($X =$ M, N, O, P) double-hole configurations the corresponding expressions are

$$\begin{aligned} \sigma'_{L_3X} = &\ \sigma_{L_1}(1 - Q_{L_1})f_{13}P(L_1\text{-}L_3X) \\ &+ \sigma_{L_2}(1 - Q_{L_2})f_{23}P(L_2\text{-}L_3X) \\ &+ \sigma_3 Q_{L_3}(X). \end{aligned} \tag{12}$$

In equations (11) and (12) σ_{L_i} are the L$_i$-subshell ionization cross-sections, Q_{L_i} is the sum of the shake-off probabilities from all possible orbitals when a hole is created in the L$_i$ subshell, f_{ij} is the partial Coster-Kronig transition probability from level L$_i$ to level L$_j$, $P(L_i\text{-}L_jX)$ is the relative probability of the radiationless transition L$_i$-L$_jX$ that results in the double vacancy state L$_jX$, and $Q_{L_3}(X)$ is the probability of shake-off from the X orbital when a hole is created in the L$_3$ subshell. It is assumed that L$_i$ vacancies always decay before the outer M holes.

Ionization cross-sections are taken from Pálinkas and Schlenk [34], for 60 keV electron impact, and shake-off probabilities are calculated in this work with MCDF wavefunctions (Tab. 3). The quantities $P(L_i\text{-}L_3X)$ in equation (12) are taken from Chen et al. [13] corresponding values for Hg, corrected for the difference in atomic number, and Coster-Kronig transition probabilities are from Chen et al. [14]. Values of σ'_{L_3X} calculated in this way are presented in the last column of Table 3.

Relative L$_3$X double-hole to L$_3$ single-hole configuration creation cross-sections are compared in Table 4 with those presented in reference [11]. Minor differences are due to shake-off values and to corrections for the atomic number, made in our calculations, in the $P(L_i\text{-}L_jX)$ values.

The X-ray production cross-sections for the diagram lines can be written as

$$\sigma^R(L_3\text{-}N_k) = \sigma'_{L_3} \frac{\Gamma(L_3\text{-}N_k)}{\Gamma^{\text{tot}}_{L_3}} \tag{13}$$

for the Lβ_2 ($k = 5$) and Lβ_{15} ($k = 4$) lines, with $\sigma'_{L_3} = 432.45$ barn, and

$$\sigma^R(L_1\text{-}M_3) = \sigma'_{L_1} \frac{\Gamma(L_1\text{-}M_3)}{\Gamma^{\text{tot}}_{L_1}} \tag{14}$$

for the Lβ_3 line, with $\sigma'_{L_1} = 139.55$ barn. In equations (13) and (14) $\Gamma(L_i - X)$ is the radiative width of the L$_i - X$ line, and $\Gamma^{\text{tot}}_{L_i}$ is the total width of the L$_i$ subshell.

Table 2. Energies in eV and transition probabilities (W) in s^{-1} for gold Lβ_2 and Lβ_{15} visible satellite lines.

L$_3$M$_5$ - M$_5$N$_5$		L$_3$M$_4$ - M$_4$N$_5$		L$_3$M$_5$ - M$_5$N$_4$		L$_3$M$_4$ - M$_4$N$_4$	
Energy	W	Energy	W	Energy	W	Energy	W
11627.05	3.38×10^{06}	11645.44	5.88×10^{11}	11614.35	4.44×10^{12}	11616.27	4.51×10^{07}
11630.44	3.69×10^{11}	11645.50	1.12×10^{12}	11614.37	9.63×10^{10}	11625.33	4.12×10^{12}
11630.50	1.25×10^{13}	11645.52	9.47×10^{10}	11614.41	1.13×10^{11}	11625.34	2.94×10^{11}
11631.65	1.28×10^{13}	11646.48	3.27×10^{08}	11614.43	3.57×10^{12}	11625.35	3.04×10^{11}
11631.71	2.85×10^{11}	11647.89	9.95×10^{11}	11615.88	6.82×10^{08}	11625.35	2.70×10^{12}
11635.82	1.91×10^{13}	11647.91	9.18×10^{12}	11617.83	2.24×10^{12}	11625.97	1.95×10^{12}
11635.84	1.34×10^{12}	11647.94	1.45×10^{13}	11617.89	1.73×10^{12}	11625.98	9.88×10^{11}
11635.90	1.37×10^{12}	11647.96	8.51×10^{11}	11617.89	6.45×10^{10}	11629.82	1.39×10^{08}
11635.93	1.22×10^{13}	11650.18	2.27×10^{12}	11621.86	1.38×10^{12}	11633.24	2.47×10^{12}
11638.60	1.16×10^{12}	11650.20	3.49×10^{13}	11621.90	2.44×10^{12}	11633.25	1.27×10^{11}
11638.66	5.08×10^{13}	11650.24	4.96×10^{13}	11621.92	2.86×10^{11}	11633.26	1.75×10^{12}
11638.70	6.23×10^{13}	11653.43	1.53×10^{08}	11623.20	1.65×10^{08}	11634.52	2.70×10^{12}
11639.27	5.04×10^{05}	11654.39	2.35×10^{12}	11624.62	2.74×10^{10}	11634.54	3.13×10^{11}
11640.46	1.06×10^{12}	11654.41	6.01×10^{13}	11624.65	1.72×10^{11}	11634.55	1.51×10^{12}
11640.46	1.38×10^{12}	11654.45	7.81×10^{13}	11624.65	2.57×10^{11}	11634.63	2.90×10^{12}
11640.52	4.36×10^{10}	11655.15	2.25×10^{12}	11624.68	1.35×10^{10}	11634.69	1.43×10^{11}
11646.62	3.07×10^{12}	11655.15	4.37×10^{12}	11626.66	1.25×10^{11}	11634.71	2.00×10^{12}
11646.69	5.16×10^{12}	11655.22	1.14×10^{13}	11626.66	2.75×10^{12}	11635.05	1.83×10^{12}
11646.69	2.86×10^{12}	11655.23	2.12×10^{12}	11626.68	1.91×10^{12}	11635.06	1.95×10^{11}
11646.71	5.90×10^{11}	11655.82	4.42×10^{11}	11633.46	5.46×10^{08}	11635.06	1.00×10^{12}
11647.32	3.55×10^{12}	11655.85	6.54×10^{11}	11634.69	5.01×10^{12}	11638.91	6.71×10^{06}
11647.38	1.72×10^{11}	11655.87	1.36×10^{10}	11634.70	1.46×10^{11}	11642.44	1.14×10^{07}
11647.46	2.46×10^{12}	11657.61	3.27×10^{12}	11634.76	3.81×10^{12}	11642.54	6.92×10^{12}
11649.22	1.05×10^{12}	11657.62	1.74×10^{13}	11636.15	3.11×10^{12}	11642.55	3.05×10^{11}
11649.25	1.49×10^{13}	11657.67	3.08×10^{13}	11636.18	2.22×10^{12}	11642.60	2.61×10^{11}
11649.29	2.13×10^{13}	11658.09	4.67×10^{11}	11636.21	1.80×10^{11}	11642.62	5.18×10^{12}
11650.77	1.21×10^{12}	11658.11	9.65×10^{12}	11638.16	1.01×10^{11}	11644.24	9.65×10^{11}
11650.83	3.16×10^{13}	11658.15	1.30×10^{13}	11638.17	2.10×10^{12}	11644.25	2.05×10^{11}
11651.99	3.29×10^{13}	11658.17	5.34×10^{11}	11638.22	1.57×10^{12}	11644.26	2.09×10^{11}
11658.25	1.85×10^{07}	11659.00	8.31×10^{12}	11638.22	9.85×10^{10}	11644.26	4.15×10^{11}
11658.93	7.78×10^{07}	11659.07	1.63×10^{13}	11646.35	9.90×10^{10}	11644.42	5.92×10^{06}
11660.33	1.06×10^{13}	11659.91	6.87×10^{09}	11646.36	2.29×10^{11}	11648.09	1.00×10^{12}
11660.42	1.19×10^{12}	11661.46	1.57×10^{09}	11646.41	5.56×10^{11}	11648.11	4.67×10^{11}
11660.43	5.88×10^{12}			11646.42	1.18×10^{11}		
11660.73	6.33×10^{11}			11649.14	1.94×10^{11}		
11660.78	1.27×10^{13}			11649.15	9.40×10^{11}		
11660.80	1.71×10^{13}			11649.17	1.75×10^{12}		
11660.85	6.47×10^{11}			11651.17	3.52×10^{08}		
11671.11	2.33×10^{12}						
11671.12	4.69×10^{12}						
11671.18	2.39×10^{12}						
11671.19	4.81×10^{12}						
11671.20	1.20×10^{13}						
11671.21	2.41×10^{12}						
11673.74	4.37×10^{07}						

Assuming that satellite lines are caused by a single Coster-Kronig transition and/or by shake-off processes, the X-ray production cross-section for each line can be expressed as

$$\sigma^{\mathrm{R}} \left(\mathrm{L}_3 X\text{-}X \mathrm{N}_k \right) = \sigma'_{\mathrm{L}_3 X} \frac{\Gamma \left(\mathrm{L}_3 X\text{-}X \mathrm{N}_k \right)}{\Gamma^{\mathrm{tot}}_{\mathrm{L}_3 X}}, \qquad (15)$$

where $\Gamma \left(\mathrm{L}_3 X\text{-}X \mathrm{N}_5 \right)$ is the radiative width of the L$_3$X-XN$_5$ transition, and $\Gamma^{\mathrm{tot}}_{\mathrm{L}_3 X}$ is the total width of the state with holes in the L$_3$ and X subshells.

Widths for L$_1$ to N$_7$ levels were taken from Campbell and Papp [32]. For the remaining one-hole levels, to our knowledge, no data are available in the literature. We used the following values $\Gamma_{\mathrm{O}_1} = 5.0$ eV, $\Gamma_{\mathrm{O}_2} = 3.8$ eV, $\Gamma_{\mathrm{O}_3} = 3.0$ eV, $\Gamma_{\mathrm{O}_4} = 2.4$ eV, $\Gamma_{\mathrm{O}_5} = 2.3$ eV, and $\Gamma_{\mathrm{P}_1} = 5.0$ eV.

Table 3. Shake-off probabilities from the X orbital when a hole is created in the L$_i$ subshell (this work) and cross-sections for creation of double L$_3X$ hole configurations in barn, for gold.

X	$Q_{L_1}(X)$	$Q_{L_2}(X)$	$Q_{L_3}(X)$	σ'_{L_3X}
K	2.82×10^{-8}	1.65×10^{-7}	3.73×10^{-8}	
L$_1$	1.11×10^{-5}	1.51×10^{-5}	1.02×10^{-5}	
L$_2$	1.25×10^{-5}	2.69×10^{-5}	1.38×10^{-5}	
L$_3$	3.05×10^{-5}	5.49×10^{-5}	3.77×10^{-5}	
M$_1$	8.95×10^{-5}	1.36×10^{-4}	1.20×10^{-4}	
M$_2$	1.63×10^{-4}	1.53×10^{-4}	1.80×10^{-4}	
M$_3$	3.60×10^{-4}	4.56×10^{-4}	3.51×10^{-4}	
M$_4$	5.26×10^{-4}	4.95×10^{-4}	5.89×10^{-4}	24.1
M$_5$	7.74×10^{-4}	8.93×10^{-4}	7.52×10^{-4}	31.9
N$_1$	3.99×10^{-4}	4.92×10^{-4}	4.68×10^{-4}	3.0
N$_2$	6.71×10^{-4}	6.37×10^{-4}	7.12×10^{-4}	7.6
N$_3$	1.44×10^{-3}	1.63×10^{-3}	1.42×10^{-3}	3.8
N$_4$	2.81×10^{-3}	2.62×10^{-3}	2.98×10^{-3}	11.4
N$_5$	4.23×10^{-3}	4.41×10^{-3}	4.16×10^{-3}	8.2
N$_6$	9.19×10^{-3}	8.87×10^{-3}	9.13×10^{-3}	7.6
N$_7$	1.22×10^{-2}	1.19×10^{-2}	1.21×10^{-2}	9.9
O$_1$	1.89×10^{-3}	2.02×10^{-3}	2.01×10^{-3}	1.7
O$_2$	3.38×10^{-3}	3.34×10^{-3}	3.46×10^{-3}	3.2
O$_3$	7.92×10^{-3}	9.07×10^{-3}	7.83×10^{-3}	4.9
O$_4$	4.11×10^{-2}	4.05×10^{-2}	4.19×10^{-2}	24.2
O$_5$	7.44×10^{-2}	7.61×10^{-2}	7.38×10^{-2}	41.4
P$_1$	7.72×10^{-2}	7.67×10^{-2}	7.66×10^{-2}	42.4
Total (Q)	2.39×10^{-1}	2.41×10^{-1}	2.39×10^{-1}	

Table 4. Relative Coster-Kronig and shake-off contributions for L$_3X$ double-hole to L$_3$ single-hole creation cross-sections, $\sigma'_{L_3X}/\sigma'_{L_3}$, for gold (%).

Spectator hole	Coster-Kronig		Shake-off	Total	Total
X	L$_1$-L$_3X$	L$_2$-L$_3X$	L$_3X$	This work	Oohashi [11]
M$_4$	5.34	0.00	0.08	5.42	5.70
M$_5$	7.07	0.00	0.10	7.17	7.60
N$_1$	0.41	0.22	0.06	0.69	0.74
N$_2$	0.17	1.50	0.09	1.76	1.80
N$_3$	0.26	0.43	0.19	0.87	0.93
N$_4$	0.64	1.60	0.39	2.63	2.70
N$_5$	0.80	0.55	0.55	1.90	2.00
N$_6$	0.51	0.07	1.20	1.77	1.80
N$_7$	0.63	0.10	1.59	2.32	2.20
O$_1$	0.08	0.04	0.26	0.39	0.39
O$_2$	0.03	0.26	0.45	0.74	0.82
O$_3$	0.05	0.07	1.03	1.15	1.20
O$_4$	0.07	0.17	5.51	5.74	15.57
O$_5$	0.08	0.06	9.69	9.83	
P$_1$	0.01	0.00	10.07	10.08	6.50

For the double-hole level widths we use $\Gamma_{XY}^{\text{tot}} = \Gamma_X^{\text{tot}} + \Gamma_Y^{\text{tot}}$, where Γ_X^{tot} and Γ_Y^{tot} are single-hole level widths.

The Lβ_{15} and Lβ_2 X-ray satellite line production cross-sections ratio relative to the Lβ_2 line are given by

$$\frac{\sigma^{\text{R}} (\text{L}_3X - X\text{N}_{4,5})}{\sigma^{\text{R}} (\text{L}_3 - \text{N}_5)} = \frac{\sigma'_{L_3X} \dfrac{\Gamma (\text{L}_3X - X\text{N}_{4,5})}{\Gamma_{\text{L}_3X}^{\text{tot}}}}{\sigma'_{L_3} \dfrac{\Gamma (\text{L}_3 - \text{N}_5)}{\Gamma_{\text{L}_3}^{\text{tot}}}}. \quad (16)$$

In equation (16) $X = $ M$_4$, M$_5$ for the visible satellites and $X = $ N$_1$ to P$_1$ for the hidden satellites. In their work, Oohashi et al. [11] assumed

$$\frac{\dfrac{\Gamma (\text{L}_3X - X\text{N}_5)}{\Gamma_{\text{L}_3X}^{\text{tot}}}}{\dfrac{\Gamma (\text{L}_3 - \text{N}_5)}{\Gamma_{\text{L}_3}^{\text{tot}}}} = 1, \quad (17)$$

Table 5. Gold Lβ_{15} and Lβ_2 satellite widths relative to Lβ_2 width (columns 2 and 3) and relative L$_3$ to L$_3X$ total level widths (column 4). In columns 5 and 6, Lβ_{15} and Lβ_2 satellite lines production cross-sections relative to Lβ_2 diagram line are presented, equation (16).

X	$\frac{\Gamma(L_3X-XN_4)}{\Gamma(L_3-N_5)}$	$\frac{\Gamma(L_3X-XN_5)}{\Gamma(L_3-N_5)}$	$\frac{\Gamma^{tot}(L_3)}{\Gamma^{tot}(L_3X)}$	$\frac{\sigma^R(L_3X-XN_4)}{\sigma^R(L_3-N_5)}$	$\frac{\sigma^R(L_3X-XN_5)}{\sigma^R(L_3-N_5)}$
M$_4$	0.118	1.024	0.72	0.0046	0.040
M$_5$	0.120	1.021	0.72	0.0061	0.053
N$_1$	0.144	0.983	0.39	0.0004	0.003
N$_2$	0.112	0.998	0.46	0.0009	0.008
N$_3$	0.160	0.952	0.52	0.0007	0.004
N$_4$	0.125	0.701	0.57	0.0019	0.011
N$_5$	0.132	0.830	0.59	0.0015	0.009
N$_6$	0.114	0.759	0.94	0.0019	0.013
N$_7$	0.099	0.890	0.94	0.0022	0.020
O$_1$	0.112	1.008	0.5	0.0002	0.002
O$_2$	0.111	0.873	0.6	0.0005	0.004
O$_3$	0.092	0.998	0.7	0.0007	0.007
O$_4$	0.105	1.109	0.7	0.004	0.044
O$_5$	0.103	0.691	0.7	0.007	0.048
P$_1$	0.111	1.000	0.5	0.006	0.053
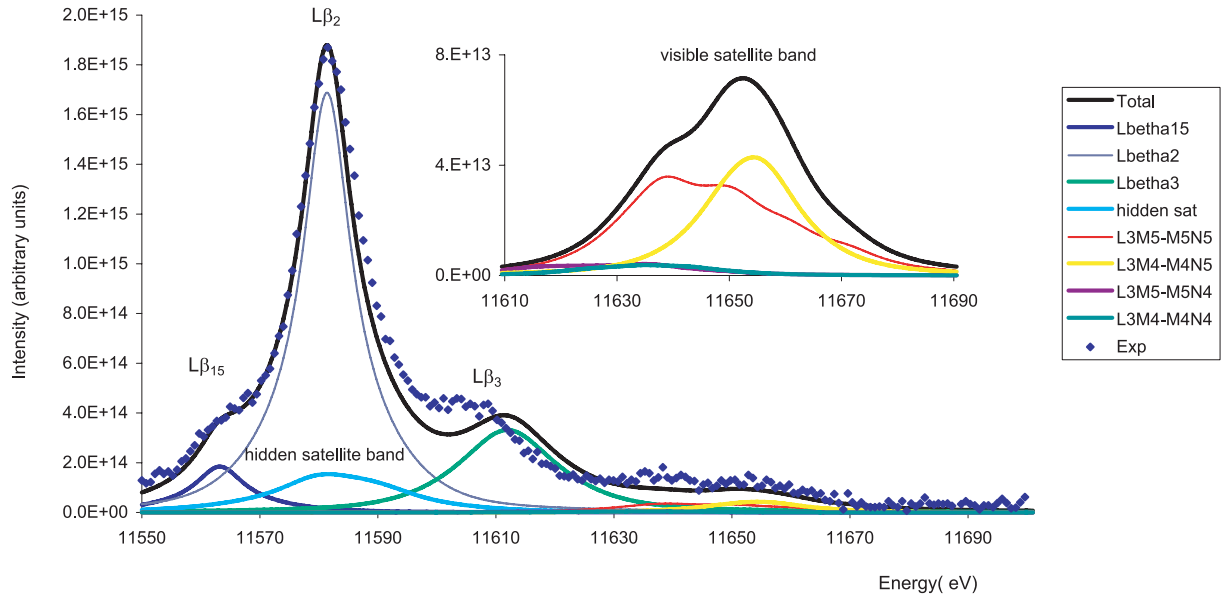
Fig. 2. (Color online) Gold L X-ray spectrum calculated in this work, including Lβ_2, Lβ_3, and Lβ_{15} diagram lines and satellite bands, compared with the experimental data (diamonds) [11]. In the inset Lβ_2, and Lβ_{15} satellite lines are shown in a different intensity scale.

allowing for a further simplification of equations. We did not use here this simplification. Instead we explicitly calculated all the contributions for the radiative linewidths both in diagram and satellite lines (Tab. 5).

The theoretical spectrum obtained using the methods discussed above and assuming, for each line, a linear combination of a Gaussian and a Lorentzian distribution, is compared with the experimental data [11] in Figure 2. To allow for a better comparison, the experimental energy was shifted by -3.2 eV in order to superimpose the Lβ_2 line in both the theoretical and measured spectra. The discrepancies between the energy values, calculated in this work, of the diagram lines and the experimental ones are

due to the neglect of correlation and other many-body corrections in our calculation [30,31,35].

3.2.3 Calculation of gold Lβ_2 satellite band using Racah's algebra

To assess the validity of the calculation of relative satellite intensities using Racah's algebra in the case of tungsten, we used the same procedure for the L$_3$M$_{4,5}$-M$_{4,5}$N$_5$ satellite bands of gold, where a more precise calculation allows for a comparison.

For gold, angular momenta that result from coupling of electrons in unfilled outer shells, in this case the 6s

Table 6. Energies and relative X-ray production cross-sections of Lβ_2 plus Lβ_{15} visible satellites for gold. Production cross-sections are relative to Lβ_2 diagram line (a) and Lβ_2 diagram line plus hidden satellites (b) production cross-sections, respectively.

| Spectator | Energy (eV) | | | Relative production cross-section (%) | | | |
hole	This work	Oohashi [11] Theory	Experiment	This work (a)	(b)	Oohashi [11] Theory	Experiment
M$_5$	11646.9	11648.4	11641.7 ± 1.1	5.9	4.6	5.5	4.1 ± 0.4
M$_4$	11654.0	11657.5	11658.7 ± 1.1	4.4	3.5	4.2	4.1 ± 0.8
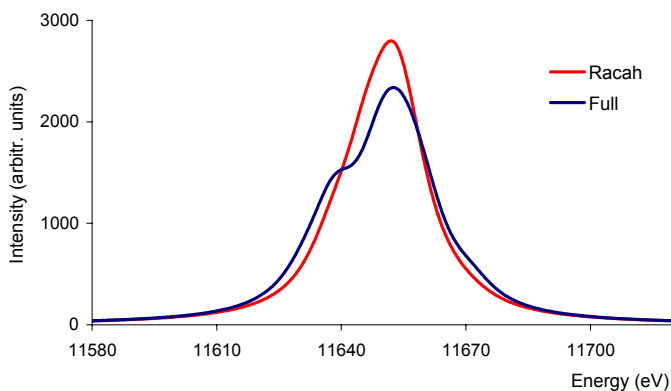
Fig. 3. Calculated satellite spectrum of gold, including the L$_3$M$_{4,5}$-M$_{4,5}$N$_5$ bands, using Multi-Configuration Dirac-Fock energy values and intensities obtained with the Racah's algebra method - Racah, and from the MCDF calculation - Full.

electron, are $j_3 = 1/2$ and $j_3' = 1/2$. Now, in what concerns equation (9), for the L$_3$M$_5$-M$_5$N$_5$ transitions we have $J = 1/2, \ldots, 9/2$ and $J' = 1/2, \ldots, 11/2$.

In order to compare the spectra generated using the two different methods, we normalized the total intensity of the L$_3$M$_5$-M$_5$N$_5$ satellite band to the same band obtained with the method described in Section 3.2.2.

The L$_3$M$_{4,5}$-M$_{4,5}$N$_5$ satellite bands thus obtained are presented in Figure 3. The agreement obtained allows us to conclude for the validity of the tungsten Lβ_2 spectrum we generated with relative intensities obtained with Racah's algebra.

4 Discussion and conclusions

In this work we computed the energy of the L$_1$-L$_3$M$_5$ Coster-Kronig transition in tungsten, using a MCDF relativistic approach. We showed that this transition is energetically allowed, thus originating Lβ_2 satellite lines. These lines had been observed 20 years ago [8] and were again observed recently [10].

The theoretical Lβ_2 satellite band of tungsten was then calculated, using MCDF relativistic transition energies and a statistical model for the shape of the band. Due to the large number of transitions involved, we were only able to estimate the position and the shape of the the Lβ_2 satellite band, using a method that employs Racah's algebra to find relative line intensities in this band. Although the experimental values suffer from very poor statistics, our results reproduce well the main features of the measured spectrum.

In the case of gold, we used the MCDF code to compute both the transition energies and the transition probabilities of the Lβ_2, Lβ_3, Lβ_{15} diagram lines as well as the Lβ_2 and Lβ_{15} satellite lines, corresponding to spectator holes in the M$_4$ and M$_5$ subshells. These satellite lines are visible satellites. We also computed the energies and transition probabilities for the hidden Lβ_2 and Lβ_{15} satellites. These are satellite lines, corresponding to spectator holes in the N$_i$ $(i = 1, 7)$, O$_i$ $(i = 1, 5)$, and P$_1$ subshells, whose energies are such that they are superimposed on the Lβ_2 diagram line.

The values found in this work for the ratio of L$_3$M$_{4,5}$-M$_{4,5}$N$_{4,5}$ to L$_3$-N$_5$ X-ray production cross-sections are presented in Table 6. For comparison with the experiment, the ratio of L$_3$M$_{4,5}$-M$_{4,5}$N$_{4,5}$ to L$_3$-N$_5$ plus hidden satellites production cross-sections were also computed. These ratios are compared with Oohashi et al. [11] theoretical and experimental values on the same table. We note that in the latter calculation, L$_3$M$_{4,5}$-M$_{4,5}$N$_4$ satellite line production cross-sections were not taken in account. Also, transition yields for satellite and diagram lines are taken by this authors as equal.

We estimate that the uncertainty in our calculation of the relative X-ray production cross-sections is of the order of 20%, due mainly to the uncertainty in the L$_1$- and L$_3$-subshells ionization cross-sections which are 20% and 10%, respectively.

The theoretical spectrum for gold obtained in this work agrees very well with experiment. Taking in account the uncertainties, the satellite bands relative intensities found in this work are consistent with the measured values of Oohashi et al. [11].

References

1. F.K. Ritchmeyer, E.G. Ramberg, Phys. Rev. **51**, 925 (1937)
2. H. Juslén, M. Pessa, G. Graeffe, Phys. Rev. A **19**, 196 (1979)
3. B.L. Doyle, S.M. Shafroth, Phys. Rev. A **19**, 1433 (1979)
4. C.F. Hague, J.-M. Mariot, G. Dufour, Phys. Lett. A **78**, 328 (1980)

5. F. Parente, M.H. Chen, B. Crasemann, H. Mark, At. Data Nucl. Data Tables **26**, 383 (1981)
6. F. Parente, M.L. Carvalho, L. Salgueiro, J. Phys. B **16**, 4305 (1983)
7. M.L. Carvalho, F. Parente, L. Salgueiro, J. Phys. B **20**, 935 (1987)
8. L. Salgueiro, M.L. Carvalho, F. Parente, J. Phys. **48**, C9-609 (1987)
9. J.Q. Xu, E. Rosato, Phys. Rev. A **37**, 1946 (1988)
10. A.M. Vlaicu, T. Tochio, T. Ishizuka, D. Ohsawa, Y. Ito, T. Mukoyama, A. Nisawa, T. Shoji, S. Yoshikado, Phys. Rev. A **58**, 3544 (1998)
11. H. Oohashi, T. Tochio, A.M. Vlaicu, Phys. Rev. A **68**, 032506 (2003)
12. T.A. Carlson, M. Krause, Phys. Rev. **140**, A1057 (1965)
13. M.H. Chen, B. Crasemann, H. Mark, At. Data Nucl. Data Tables **24**, 13 (1979)
14. M.H. Chen, B. Crasemann, K.-N. Huang, M. Aoyagi, H. Mark, At. Data Nucl. Data Tables **19**, 97 (1977)
15. B.K. Agarwal, *X-Ray Spectroscopy* (Springer-Verlag, Berlin, 1979), 210
16. J.P. Desclaux, in *Methods and Techniques in Computational Chemistry* (STEF, Cagliary, 1993), Vol. A
17. P. Indelicato, Phys. Rev. Lett. **77**, 3323 (1996)
18. MCDFGME, a MultiConfiguration Dirac Fock and General Matrix Elements program, (release 2005), written by J.P. Desclaux, P. Indelicato (`http://dirac.spectro.jussieu.fr/mcdf`)
19. K. Dyall, I.P. Grant, C.T. Johnson, F.A. Parpia, E.P. Plummer, Comp. Phys. Commun. **55**, 425 (1989)
20. O. Gorceix, P. Indelicato, Phys. Rev. A **37**, 1087 (1988)
21. E. Lindroth, A.-M. Martensson-Pendrill, Phys. Rev. A **39**, 3794 (1989)
22. W.R. Johnson, G. Soff, At. Data Nucl. Data Tables **33**, 405 (1985)
23. P.O. Löwdin, Phys. Rev. **97**, 1454 (1955)
24. P. Indelicato, Phys. Rev. A **26**, 2338 (1982)
25. P.J. Mohr, Y. Kim, Phys. Rev. A **45**, 2727 (1992)
26. P.J. Mohr, Phys. Rev. A **46**, 4421 (1992)
27. P.J. Mohr, G. Soff, Phys. Rev. Lett. **70**, 158 (1993)
28. P. Indelicato, O. Gorceix, J.P. Desclaux, J. Phys. B **20**, 651 (1987)
29. P. Indelicato, J.P. Desclaux, Phys. Rev. A **42**, 5139 (1990)
30. P. Indelicato, E. Lindroth, Phys. Rev. A **46**, 2426 (1992)
31. P. Indelicato, S. Boucard, E. Lindroth, Eur. Phys. J. D **3**, 29 (1998)
32. J.L. Campbell, T. Papp, At. Data Nucl. Data Tables **77**, 1 (2001)
33. M.O. Krause, F. Wuilleumier, C.W. Nestor Jr, Phys. Rev. A **6**, 871 (1972)
34. J. Pálinkas, B. Schlenk, Z. Physik A **297**, 29 (1980)
35. R.D. Deslattes, E.G. Kessler Jr, P. Indelicato, L. de Billy, E. Lindroth, J. Anton, Rev. Mod. Phys. **75**, 35 (2003)